

Amyloid-like DNA bridging: a new mode of DNA shaping

Frank Wien^{1,†}, Marcos Gragera^{2,†}, Tatsuhito Matsuo^{3,4,5,†}, Gautier Moroy⁶,
María Teresa Bueno-Carrasco², Rocío Arranz², Antoine Cossa⁷, Anne Martel³,
Heloisa N. Bordallo⁸, Svemir Rudić⁹, Marisela Velez¹⁰, Johan R.C. van der Maarel¹¹,
Judith Peters^{12,3,5,12}, Véronique Arluison^{13,*}

¹Synchrotron SOLEIL, L'Orme des Merisiers, Saint Aubin BP48, 91192 Gif-sur-Yvette, France

²Centro Nacional de Biotecnología (CNB-CSIC), 28049 Madrid, Spain

³Institut Laue-Langevin, 71 avenue des Martyrs, CS 20156, 38042, Grenoble Cedex 9, France

⁴Hiroshima International University (HIU), Hiroshima 739-2695, Japan

⁵Université Grenoble Alpes, CNRS, LiPhy, 38000 Grenoble, France

⁶Université Paris Cité, CNRS, INSERM, Unité de Biologie Fonctionnelle et Adaptative, F-75013 Paris, France

⁷Laboratoire Léon Brillouin LLB, UMR12 CEA CNRS, CEA Saclay, 91191 Gif-sur-Yvette, France

⁸The Niels Bohr Institute, University of Copenhagen, DK-2100 Copenhagen, Denmark

⁹ISIS Neutron and Muon Source, SFTC, Rutherford Appleton Laboratory, Didcot OX11 0QX, United Kingdom

¹⁰Instituto de Catálisis y Petroleoquímica (CSIC), c/Marie Curie 2, Cantoblanco, Madrid 28049, Spain

¹¹Department of Physics, National University of Singapore, 117542, Singapore

¹²Institut Universitaire de France, 75005 Paris, France

¹³Université Paris Cité, UFR SDV, 75006 Paris, France

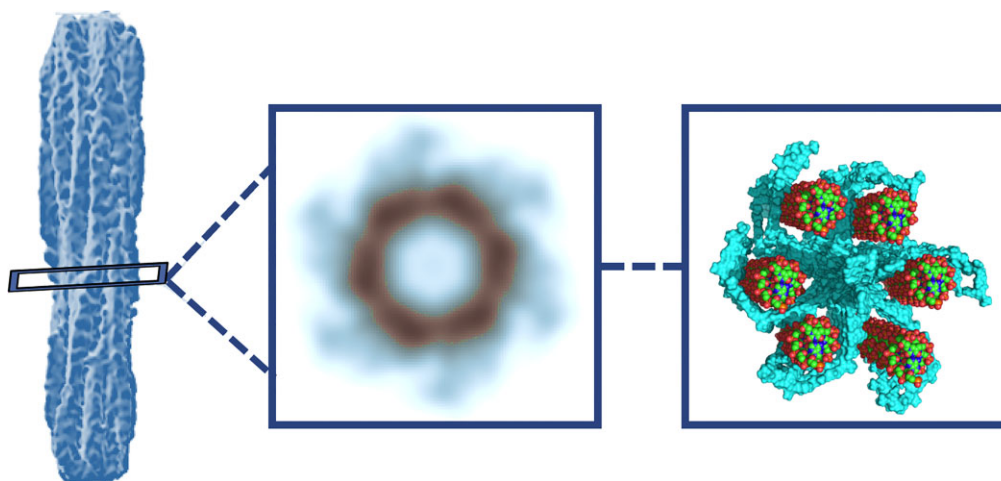
*To whom correspondence should be addressed. Email: veronique.arluison@u-paris.fr

†The authors wish it to be known that, in their opinion, the first three authors should be regarded as Joint First Authors.

Abstract

All organisms depend on specific proteins to compact and organize their genomes. In eukaryotes, histones fulfil this role, while bacterial chromosomes are shaped by nucleoid-associated proteins (NAPs). Among its pleiotropic functions, the NAP Hfq plays a pivotal role in bacterial genome organization. In this study, we characterized the structure of the C-terminal extension of Hfq, which mediates chromosomal compaction, in its DNA-bound state. Using an integrative approach that combined transmission electron microscopy, neutron scattering, site-directed mutagenesis, and molecular modeling, we identified an amyloid module formed by the C-terminal region of Hfq. This module uniquely bridges and compacts six DNA molecules, marking the first documented instance of an amyloid structure with DNA-bridging properties. Our findings redefine the functional landscape of amyloids, linking them to genome architecture and gene regulation. This result suggests that amyloid-DNA interactions may represent a conserved mechanism across biological systems, with profound implications for understanding genome organization and the regulation of gene expression in both prokaryotes and eukaryotes.

Graphical abstract



Received: December 11, 2024. Revised: February 5, 2025. Editorial Decision: February 19, 2025. Accepted: February 23, 2025

© The Author(s) 2025. Published by Oxford University Press on behalf of Nucleic Acids Research.

This is an Open Access article distributed under the terms of the Creative Commons Attribution-NonCommercial License

(<https://creativecommons.org/licenses/by-nc/4.0/>), which permits non-commercial re-use, distribution, and reproduction in any medium, provided the

original work is properly cited. For commercial re-use, please contact reprints@oup.com for reprints and translation rights for reprints. All other

permissions can be obtained through our RightsLink service via the Permissions link on the article page on our site—for further information please contact

journals.permissions@oup.com.

Introduction

In bacteria, the genome is highly compacted despite the lack of a nuclear membrane [1]. The bacterium *Escherichia coli*, for example, has a chromosome typically consisting of 4.5–5.5 millions base pairs, which corresponds to a total length of ~ 1.5 mm [2]. This must be compacted to fit within a cell volume of $\sim 1 \mu\text{m}^3$. This compaction is made possible by proteins organizing the DNA into a dense structure known as the nucleoid. The bacterial proteins responsible for shaping DNA are collectively referred to as nucleoid-associated proteins (NAPs) [1]. In *E. coli*, ~ 10 proteins are recognized as NAPs, using various mechanisms to influence the DNA structure [3]. NAPs can alter the shape of DNA by bridging, bending, or stiffening it. Consequently, NAPs can influence transcription by either promoting or preventing RNA polymerase (RNAP) access to the DNA. For instance, RNAP can be inhibited in two main ways: the binding of RNAP to promoters can be blocked due to DNA occupancy by NAP and transcription elongation can be paused by DNA-bridged complexes. Additionally, DNA supercoiling affects the opening of loops during transcription and replication, and NAPs also play a role in this process. Finally, NAPs help to constrain DNA into a condensed form, preserving its integrity and enabling repair when DNA breaks occur.

Among *E. coli* NAPs, the best-known and most characterized are HU (heat-unstable nucleoid protein) and H-NS (histone-like nucleoid structuring protein). The concentration of HU can reach up to 30 000 copies per cell, and it binds DNA cooperatively to form a rigid filament, increasing its persistence length and resulting in high bending radius and torsion [4]. In contrast, H-NS, with ~ 20 000 copies per cell, prefers to bind to curved and/or AT-rich regions [5]. H-NS is capable of multimerizing to form a rigid filament along the DNA, similarly to HU [6], but, unlike HU, it does not bend DNA. Instead, H-NS bridges two DNA strands together, bringing distant loci into close proximity [6, 7].

Here, we focus on another bacterial protein belonging to the DNA-bridging proteins, the *E. coli* Hfq (Host factor Q-beta) [8]. Hfq was identified as a NAP ~ 25 years ago [9, 10]. Its abundance is similar to that of H-NS and HU. However, its precise role in DNA shaping remained unclear for years. Indeed, its best-characterized function is in RNA metabolism, particularly in the regulation using small noncoding RNAs (sRNAs) [11, 12]. Although Hfq's affinity for RNA is much higher than its affinity for DNA (equilibrium dissociation constant K_D in the pM range for RNA versus nM for DNA) [13–15], $\sim 20\%$ of the total cellular concentration of Hfq is found within the nucleoid [16]. The average concentration of Hfq in the nucleoid is ~ 10 – $15 \mu\text{M}$, and its local concentration can reach tens to hundreds of μM [9, 16].

While Hfq is a member of DNA-bridging proteins, similar to H-NS, its mechanism of bridging differs. Unlike H-NS, which uses a coiled-coil structure for bridging and polymerizing along the DNA, Hfq employs an amyloid-like region for this function. Structurally, Hfq consists of two distinct domains: an oligomeric N-terminal region (NTR) adopting an Sm-fold, which is composed of an α -helix capped by a five-stranded bent antiparallel β -sheet. The β -sheets β_4 and β_5 from two consecutive monomers assembled to form an oligomeric torus, a hexamer [11]. In addition to the NTR, *E. coli* Hfq has a C-terminal domain (CTR), which extends beyond the toroidal Sm-core [17]. Furthermore, while Hfq proteins from different bacteria exhibit an evolutionarily con-

served Sm-NTR, there is considerable variation at the C-terminal end of the protein [18]. For instance, the CTR is absent in some bacteria, such as *Staphylococcus aureus* Hfq [19], whereas in other species, like *Acinetobacter baumannii*, Hfq harbors an exceptionally long CTR [20]. In *E. coli*, an amyloid-like structure is found within the CTR [21, 22], specifically in the 11 amino acid residues at the very end of the protein [23].

We previously observed that the isolated CTR of Hfq binds DNA independently of the NTR, and that DNA induces amyloidogenesis [24, 25]. The isolated CTR peptide is referred here to as Hfq-CTR. We have also reported that Hfq-NTR alone, which forms the hexameric torus, binds DNA, though this binding is significantly reinforced by the C-terminal arm, resulting in cooperative binding [15]. Furthermore, the full-length Hfq can also polymerize into well-ordered amyloid fibers, which are capable of binding nucleic acids [26]. The amyloid region of Hfq allows the compaction of double-stranded (ds) DNA both *in vitro* and *in vivo* [15, 27, 28]. However, to date, no 3D structure has been available for the Hfq-CTR, either as a single peptide or in a complex with DNA. Only the structure of a complex between the NTR region of Hfq and DNA has been solved [29]. The lack of a 3D structure for Hfq-CTR is likely due to the complexity of obtaining an atomic structure for an amyloid region, especially when it forms a large, flexible super-structure [30].

Cryo-electron microscopy (cryo-EM) methods have recently become a preferred approach for analyzing amyloid fibers [31], achieving resolutions down to a few Å. Cryo-preservation allows the sample to be observed in a vitrified, close-to-native state, without the need for staining or chemical fixation, thus preserving its natural structure. In this work, we present the first cryo-EM structure of the fibrillar complex of DNA and Hfq-CTR (henceforth referred to as fiber), revealing a novel mode of DNA bridging. These EM results are complemented by atomic force microscopy (AFM) and small-angle and inelastic neutron scattering (SANS/INS) measurements. By using contrast variation, SANS enables to highlight only one component while suppressing the contribution of the other component of the complex [32], while INS allows to follow the dynamical response of the hydrated complex. Together, these findings provide new insights into bacterial DNA compaction and shed light on the possible expanding role of pathological amyloids, implicated in neurodegenerative diseases, in the regulation of gene expression [33, 34].

Materials and methods

Sample preparation

The sample analyzed consisted of the amyloid structure formed by the Hfq-CTR peptide (38 amino acid residues) bound to a dsDNA sequence: (dA:dT)₅₉. The choice of this 59-basepair homo-polymeric DNA sequence was made because Hfq has highest affinity for A-rich sequences *in vitro* and *in vivo* [8, 14]. The Hfq-CTR (residues 66–102 of full-length Hfq), and the dsDNA sequence were chemically synthesized (Proteogenix/France and Eurogentec/Belgium, respectively). The sequence of the peptide was SRPVSHH-SNNAGGGTSSNYHHGSSAQNTSAQQDSEETE. The fiber was reconstituted in water (H₂O) or deuterated water (D₂O) for SANS analysis. We determined that pH ~ 5 was most appropriate for complex formation [24]. Note that at the chosen concentration, the peptide shows self-buffering properties.

The molar ratio DNA base pair to Hfq-CTR peptide was 4:1, as used in our previous analyses (DNA concentration is expressed in base-pairs/L) [25]. Samples were analyzed after 4 weeks to allow complex full self-assembly. The same solutions used for SANS in H₂O were used for cryo-TEM analysis. Note that, due to the hinge between the Hfq-NTR and CTR domains, the assembly of full-length Hfq with DNA was too flexible to be analyzed using the methods described below.

Cryo-transmission electron microscopy (cryo-EM)

Cryo-EM sample preparation

Cryo-transmission electron microscopy (cryo-EM) analysis was performed on the CryoEM facility at the National Centre for Biotechnology (Centro Nacional de Biotecnología of the Spanish National Research Council CNB-CSIC, Madrid, Spain) with an iNEXT-Discovery proposal (PID: 19 663). Cryo-EM grids of the fiber prepared in water were vitrified using a FEI Vitrobot Mark IV (ThermoFisher, Waltham, MA, USA). Quantifoil Cu/Rh 2/2300 mesh grids (Quantifoil, Jena, Germany) were previously glow-discharged for 30 s at 25 mA. Aliquots of 3 μ l of the sample were added onto the grids, blotted for 3 s at 4°C and 95% humidity, and plunged into liquid ethane.

Cryo-EM data collection

Screening and data acquisition of the sample were performed using a 200 kV FEI Talos Arctica (ThermoFisher, Waltham, USA) equipped with a Falcon III direct electron detector (ThermoFisher, Waltham, MA, USA). A total of 1137 movies of the fibers were acquired at a nominal magnification of $\times 73\,000$ (corresponding to a pixel size of 1.37 Å/pixel), with a defocus range of -1.2 to -3.1 μ m. Movies were fractionated to 40 frames with a total exposure of 40 s and a total dose per movie of 40 e⁻/Å².

Cryo-EM data analysis

The set of movies acquired through the iNEXT project was then subjected to single particle analysis (SPA). The image processing pipeline proceeded as follows: movies acquired on the 200 kV Talos Arctica were aligned using MotionCorr [35]. Then, micrographs were imported in cryoSPARC [36] for further processing. Contrast transfer function (CTF) was estimated with CTFFIND4 [37]. An initial picking was carried out using Filament Tracer, setting 8 and 20 nm of minimum and maximum diameter, respectively, and a separation distance of 1 diameter. A total of 34 867 particles were extracted with an 800 px box-size and Fourier-cropped to 400 px, followed by several rounds of 2D classification. 2D averages showing structural detail were used as templates for an additional round of picking with Filament Tracer (filament diameter: 18 nm, 1 diameter of separation distance), resulting in 59 043 particles. These particles were extracted in a 580 px box-size and subjected to several rounds of 2D classification up to a final number of 27 059 particles. Due to the lack of resolution in the power spectra, helical parameters could not be reliably determined. Therefore, the final 3D map was obtained with asymmetric helical refinement, at 19 Å resolution (gold-standard FSC at 0.143 cut-off criterion).

Symmetry analysis

For symmetry analysis, we selected a straight region of the electron density along the helical axis, averaged 100 slices (396–495) perpendicular to this axis, computed the average projection and applied symmetries from 3- to 10-fold. The cross-correlation coefficient between each symmetrized image and the average projection were determined to identify the best fitted symmetry.

Atomic force microscopy

The fibers in water were diluted and incubated on freshly cleaved mica for 15–30 min. Non adsorbed fibers were removed from solution through extensive rinsing, and the images were taken with the mica substrate immersed in distilled water. Tapping mode images were acquired with an atomic force microscope from Agilent Technologies 5500 (Agilent technology, Santa Clara, CA, USA). All images were recorded at room temperature employing rectangular gold-coated cantilevers with silicon nitride tips with a tip diameter, nominally, of <10 nm, and a nominal spring constant of 0.28 Nm⁻¹ and resonant frequency of 66 kHz in air HYDRA6R (AppNano, Mountain View, CA, USA). Data acquisition and analysis were performed using PicoView 1.3 (Agilent Technologies, Santa Clara, CA, USA) and WSxM 5.0 Develop 8.0 [38], respectively.

Small angle neutron scattering

A set of samples was prepared by dissolving the fibers in mixtures of H₂O and D₂O to a DNA and Hfq-CTR concentration of 15 and 3.75 g/l, respectively (molar ratio DNA bp:Hfq-CTR 4:1). Highly viscous samples were loaded into banjo-type quartz cells (Hellma, Germany) [39]. We applied contrast variation with four solvent compositions: 0%, 34%, 51% (Hfq-CTR matched), and 100% D₂O. Small angle neutron scattering (SANS) was measured at 298 K with the large dynamic range small-angle diffractometer D22 at the Institute Laue Langevin (ILL) in Grenoble (France). A wavelength of 0.6 nm with a 10% spread was selected and the sample-to-detector distances were 1.4 m for the fixed detector and 5.6 m and 17.6 m for the mobile detector, with collimation lengths equal to the long sample-to-detector distance in each configuration. The total counting time for all detector settings was ~ 2 h per sample. Data reduction using Grasp software allowed subtraction of background scattering (empty cell and blocked beam), as well as sample transmission and thickness scaling, and detector pixel efficiency correction. Grasp is a MATLAB script application designed for the graphical inspection, analysis, and reduction of multi-detector data produced by SANS instruments at the ILL (<https://www.ill.eu/users/support-labs-infrastructure/software-scientific-tools/grasp>). The efficiencies of the detector pixels were determined using the scattering of H₂O. Absolute intensities were obtained with reference to the directly measured incident flux, and the scattering of the sample cell with solvent at the same isotopic composition was subtracted. The scattering contributions pertaining to DNA and Hfq-CTR (partial structure factors) were then obtained by a simultaneous two-parameter fit to the data from the four solvent compositions [40, 41].

Inelastic neutron scattering

INS was used to measure molecular vibrations and revealed details of the shapes of interaction potentials in the fiber. Here, the dynamics of crystalline D₂O ice Ih (buffer), D₂O + DNA, D₂O + Hfq-CTR, and D₂O + Hfq-CTR + DNA were studied at 10 K by using the spectrometer TOSCA at the ISIS Neutron and Muon Source at the Rutherford Appleton Laboratory (United Kingdom) [42]. A solution of 10 g/l of DNA (corresponding to 0.0152 mol/l of DNA expressed in base pair) and 15.15 g/l of Hfq-CTR (corresponding to 0.0038 mol/l of peptide) were prepared. The ratio DNA: Hfq-CTR was thus 4:1, like in our previous analyses (cryoTEM, SANS). The sample volume was ~2 ml for each sample.

TOSCA is an indirect geometry time-of-flight neutron spectrometer with a fixed final energy of the neutrons for observing vibrational spectra in neutron energy loss. The instrument covers the entire frequency range for molecular vibrations. INS spectra for all samples were converted into the incoherent dynamics structure factor, $S(q, \omega)$ using Mantid software [43]. As part of data reduction, the spectra are automatically normalized in relation to the proton beam current, and the signal coming from the empty aluminum sample holder was subtracted. It is important to recall that the spectra of hydrogen containing materials measured on TOSCA are dominated by vibrational motions of the hydrogen atoms, since their incoherent cross section (σ_H) is at least a factor of ten times larger than that of most elements in bio-samples [44]. Thus, in its simpler form, the measured inelastic scattering is dominated by self-correlations in atomic motions [45] and can be written as [46]:

$$S(q, n\omega_i) \propto (q \cdot U_i)^2 \exp[-(q \cdot U_{\text{total}})^2] \sigma_H \quad (1)$$

where U_i is the zero-point displacement of the H-atom due to the mode ω_i , and U_{total} is the total displacement of the H-atom with all modes. The exponential term in equation (1) is the Debye–Waller factor, which is directly related to the structure flexibility, i.e. lower mobility is indicated by a reduced mean-square displacement and vice versa. Thus, INS allows for a direct investigation of protein conformational changes because the large-amplitude motions involved in the process are in the right frequency range measured by the technique.

Molecular visualization

The DNA and Hfq-CTR peptides were built using the PyMOL program (The PyMOL Molecular Graphics System, Version 3.0 Schrödinger, LLC; available online: <https://pymol.org/>). The DNA double helix monomers were arranged in a hexagonal arrangement based on TEM projection, with a 3.8 nm spacing between each of the monomers. The Hfq-CTR peptides have been manually positioned between the DNA double helix monomers taking into account: (i) the region necessary to form the amyloid structure [23] and (ii) the residues previously identified to bind DNA [24]. The position of the DNA strands in the CryoTEM envelope was optimized using the “Fit in Map” tool implemented in the Chimera program [47]. The figures were generated using PyMOL.

Results

First, we analyzed the fibrillar complex of Hfq-CTR and DNA at room temperature (RT) using the AFM. Images revealed fibers with a rod-like structure extending over at least a mi-

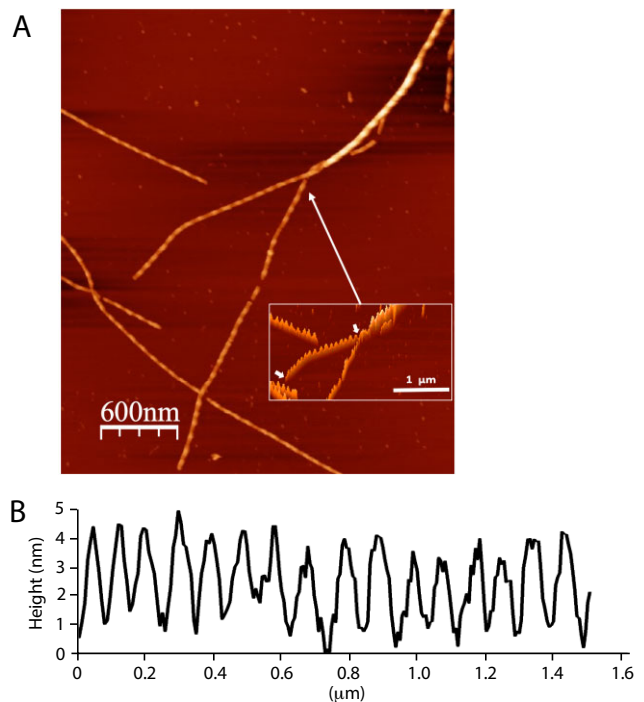


Figure 1. AFM images of fibrillar Hfq-CTR:DNA complexes on mica. **(A)** Fibers adopting a helical structure. Note the tendency of the fibers to intertwine at the top of the panel. The inset shows a tilted view of long fibers, revealing 2–3 nm protrusions spaced by ~100 nm. **(B)** The profile of the top of the fiber, taken from the region indicated by the two white arrows.

cron in length (Fig. 1A). The fibers exhibit regions of different widths that extend periodically all along the fibers. The cross-sectional width ranges from 30 to 35 nm, while the measured height is ~5–10 nm, suggesting that the fibers could be flattened on the surface, despite that the images were taken in solution. Indeed, we cannot rule out a flattening effect due to the interaction with the mica, or that the width of the tip could contribute to the measured width of the fibers. Note that the fibers exhibit a tendency to intertwine as shown on the top of Fig. 1A. A helical repeat with a pitch of 80–100 nm is observed along the fibers (Fig. 1B).

Fibers were also studied using cryo-EM, which allowed the examination of structural features in more detail, complementing the observations made by the AFM. Cryo-EM micrographs revealed at least two winding types of helical fibers (Fig. 2). On average, the fibers have a diameter of 10–15 nm and the pitch of the helix formed is ~100 nm. These mean helical parameters are in agreement with measurements made using liquid AFM. As for AFM analysis, we also observed by TEM two types of fibers, namely “basic” fibers, the ones that have been reconstructed, but also thicker fibers, up to 25 nm thick, most likely two thin fibers winding around each other(s) to form the thicker one (Supplementary Fig. S1). Both the mean helical parameters and interwinding of fibers are in agreement with AFM results and thus indicate that the structure observed at cryogenic temperature is the same as than the one observed at room temperature.

Next, the cryo-EM dataset was subjected to helical reconstruction in order to obtain a 3D volume of the fiber at nanometric resolution. The final 3D volume, shown in Fig. 3A and B, was obtained using asymmetric helical refinement, as the

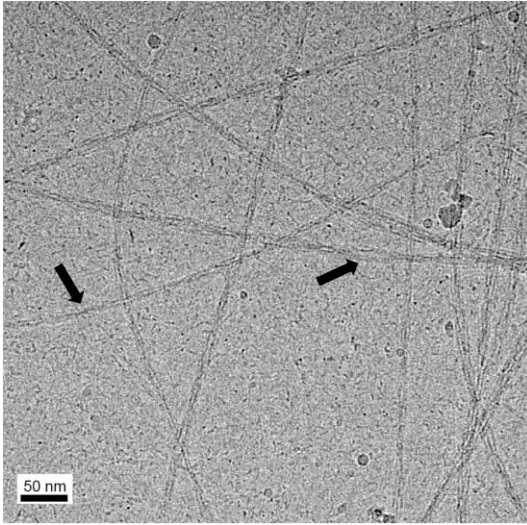


Figure 2. Cryo-EM image of the Hfq-CTR:DNA fibers. Representative aligned micrograph from a set of 1100 movies acquired. Arrows indicate the two kinds of fibers found in this work: thin fibers (10–15 nm diameter) and thicker fibers (25 nm diameter). The scale bar represents 50 nm.

helical parameters could not be reliably determined from the power spectra of the 2D averages due to limited resolution of the micrographs. Consequently, the resolution of the reconstruction was 19 Å. Given that distance measured directly on the micrograph may be inaccurate due to CTF-induced artifacts, the diameters of isolated fibers were measured both directly from the 2D averages (Supplementary Fig. S2) and from the 3D reconstruction after asymmetric helical refinement. Measurements from the 2D averages ranged from ~8.5 nm in the thinnest regions to 16.5 nm in the thickest. In the 3D volume, the shortest and longest diameters measured were 8.9 and 15 nm, respectively.

Next, a symmetry analysis of the fiber was performed. For this, we selected a straight region of the electron density along the helical axis, averaged 100 slices perpendicular to this axis, and computed the average projection. We then applied symmetries ranging from 3- to 10-fold. Cross-correlation coefficients between each symmetrized image and the average projection were calculated, and the best fit was found with a 6-fold symmetry, indicating that the fiber tends to adopt a hexameric structure globally (Fig. 3C). Although a 10-fold symmetry could not be ruled out, it is less probable. Note that this possibility can be explained by the dissociation of dsDNA into single-stranded regions, which would result in the presence of more DNA strands (see below).

While cryo-EM provides insight into the overall structure of the fiber, the exact nature of the various densities observed in the cryo-EM images cannot be definitively attributed from the 3D density alone. To perform a more detailed structural analysis of the nucleoprotein complex, we conducted low-resolution small-angle neutron scattering (SANS) experiments with contrast variation (Fig. 4). By varying the scattering contrast parameters, SANS allows for the enhancement of one component while minimizing the contribution of another in a complex. In this case, it was used to isolate the individual scattering contributions from DNA and Hfq-CTR within the fibrillar complex. The cross-sectional form factors for DNA and Hfq-CTR are shown in Fig. 4A and D, respectively, as functions of

the momentum transfer between the neutron and the scattering atom, q . The momentum transfer q is defined by the wavelength λ of the radiation and the scattering angle θ between the incident and scattered beams, according to the equation $q = 4\pi/\lambda \sin(\theta/2)$. The form factors were obtained by multiplying the scattering contributions from DNA and Hfq-CTR (partial structure factors) by q to account for the local rod-like structure, and they were normalized to unity at $q = 0$. It is assumed that the data are not affected by interference between different fibers for q values exceeding 0.1 nm^{-1} . As q increases, the form factors gradually decrease until reaching a minimal value, followed by a subsequent maximum at higher momentum transfer values. Notably, the minimum in the DNA form factor occurs at a lower q -value than that of the Hfq-CTR form factor, indicating that the Hfq-CTR is distributed at smaller radial distances within the fiber compared to DNA. This results from bridging of the DNA helices. The cryo-EM micrographs reveal that the fiber exhibits a cross-sectional hexagonal symmetry, with individual DNA strands forming both inner and outer layers. The DNA molecules in the outer layer appeared to be twisted away from the fiber's long axis, as indicated by the helical pitch observed in both AFM and cryo-EM images. This pitch, ~100 nm, exceeds the observation window for $q > 0.1 \text{ nm}^{-1}$. For two coaxial layers of DNA arranged in a hexagonal grid with transverse offsets r_{in} and r_{out} , the cross-sectional form factor is given by [48]:

$$P_{DNA} = [\rho_{in}^c(q)J_0(qr_{in}) + \rho_{out}^c(q)J_0(qr_{out})]^2/4$$

Here, $\rho_i^c(q)$ denotes the Hankel transform of the cross-sectional DNA strand profile (where $i = in, out$). For a Gaussian profile, $\rho_i^c(q)$ is given by $\rho_i^c(q) = \exp(-q^2\sigma_i^2/4)$ with width σ_i . The form factor expression was fitted to the DNA data using Mead-Nelder optimization of the transverse offsets and widths of the DNA strands. As shown in Fig. 4A, the model fits the data excellently. Figure 4B and C display the resulting two-dimensional density distribution of the cross-section and the azimuthally averaged radial density profile, respectively. The transverse offset of the DNA molecules in the inner layer, r_{in} , is 3.8 nm. The inner layer has a cross-sectional width, $\sigma_{in} = 0.7 \text{ nm}$, which is close to the radius of dsDNA in the B-form [40, 41]. The transverse offset of the outer layer, r_{out} , is 8 nm, with a cross-sectional width of $\sigma_{out} = 3 \text{ nm}$. The inner and outer layers are separated at a radial distance of 6 nm. Consequently, the outer layer is more diffuse, in agreement with the cryo-EM micrographs. The total diameter of the fibers is ~20 nm (resulting from an average of simple A and double fibers B, Supplementary Fig. S1).

For the analysis of the cross-sectional form factor of Hfq-CTR, we assumed a two-layered structure, while neglecting any potential inhomogeneous distribution in the azimuthal direction. The radial density profile of Hfq-CTR was modeled as the sum of two Gaussians, with offsets and widths denoted as (r_{in}, σ_{in}) and (r_{out}, σ_{out}) , respectively. The relative contributions of these layers were then optimized. As shown in Fig. 4D, the model fits the data well. Figure 4E and F present the two-dimensional isotropic density distribution and the radial density profile, respectively. The inner layer, which contributes 95% of the radial Hfq-CTR density, has a transverse offset of $r_{in} = 2 \text{ nm}$ and a width of $\sigma_{in} = 2 \text{ nm}$. The minor contribution from the outer layer is offset by $r_{out} = 8 \text{ nm}$ and has a width of $\sigma_{out} = 2 \text{ nm}$. These results confirm that the Hfq-CTR wraps the DNA strands with a density pro-

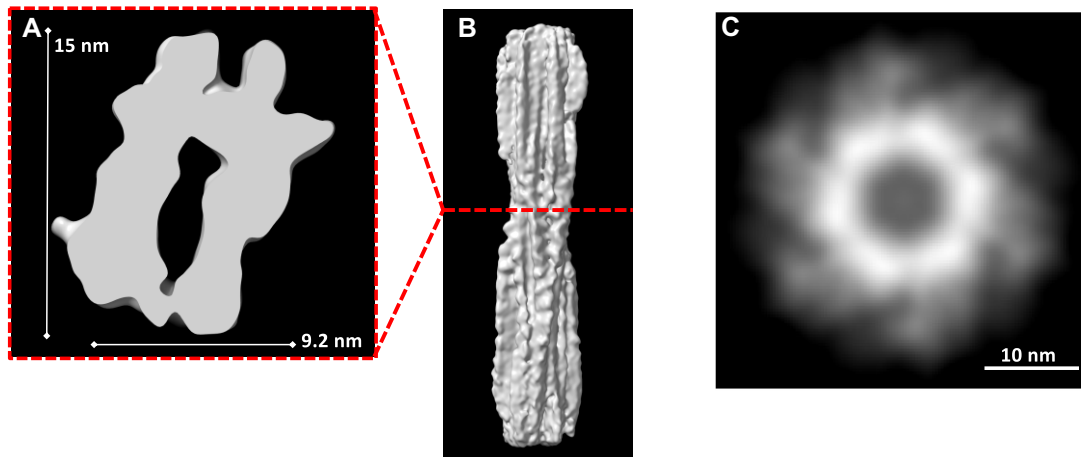


Figure 3. Asymmetrical helical reconstruction of the fiber using SPA. **(A)** Close-up view of a section in the thinner part of 3D reconstruction, as shown in panel **(B)**. **(C)** Symmetry analysis of the 3D reconstructed fiber. A 6-fold symmetry is observed for the reconstructed fiber, with slight outward deformation confirming the right-handed helical nature of the fiber.

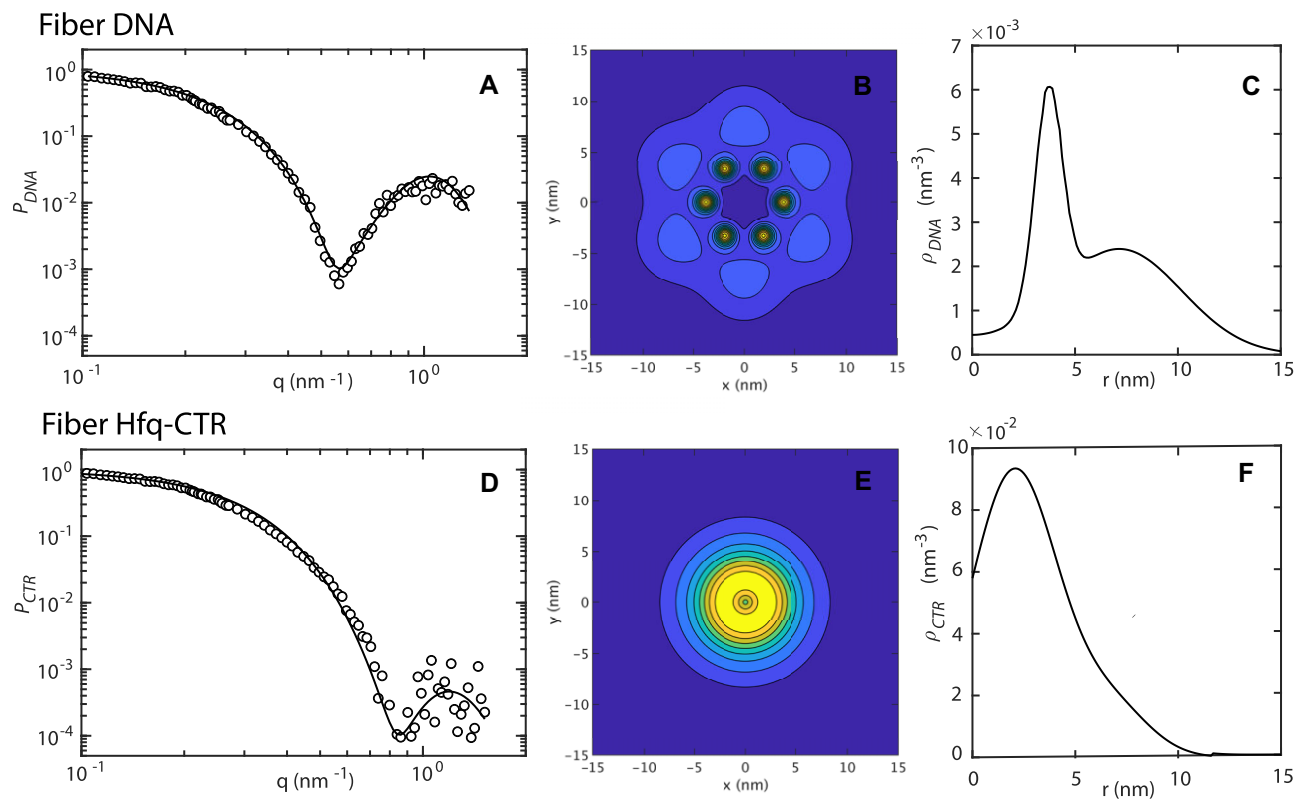


Figure 4. SANS analysis. **(A)** Cross-sectional form factor for the DNA component of the fiber. The solid curve represents the fit of the form factor expression. **(B)** Two-dimensional DNA density profile of the fiber's cross-section. **(C)** Azimuthally averaged radial DNA density profile. **(D-F)** As in panels **(A-C)** but for the Hfq-CTR component.

file extending across the full cross-sectional range of the fiber, with maximal density in the inner region due to limited space availability.

We have now confirmed that six DNA molecules are packed together by the Hfq-CTRs. However, as noted earlier, some bifurcations are observed in the cryo-EM reconstruction. We suspect that these bifurcations result from the Hfq-induced dissociation of dsDNA into single strands, as reported earlier [8].

To test this hypothesis, we performed INS experiments ([Supplementary Fig. S3](#)). First, considering that the vibrational region between 330 and 480 cm^{-1} probes the deuterated water molecules hydrating the protein [49], we conclude that the shift in the D_2O vibration at 400 cm^{-1} is a direct spectroscopic signature of bound water molecules. This signature remains unchanged when comparing the complexes (Fig. 5A). Furthermore, the absence of vibrations in the 900 cm^{-1} region confirms that no H/D exchange occurred in this study [50]. There-

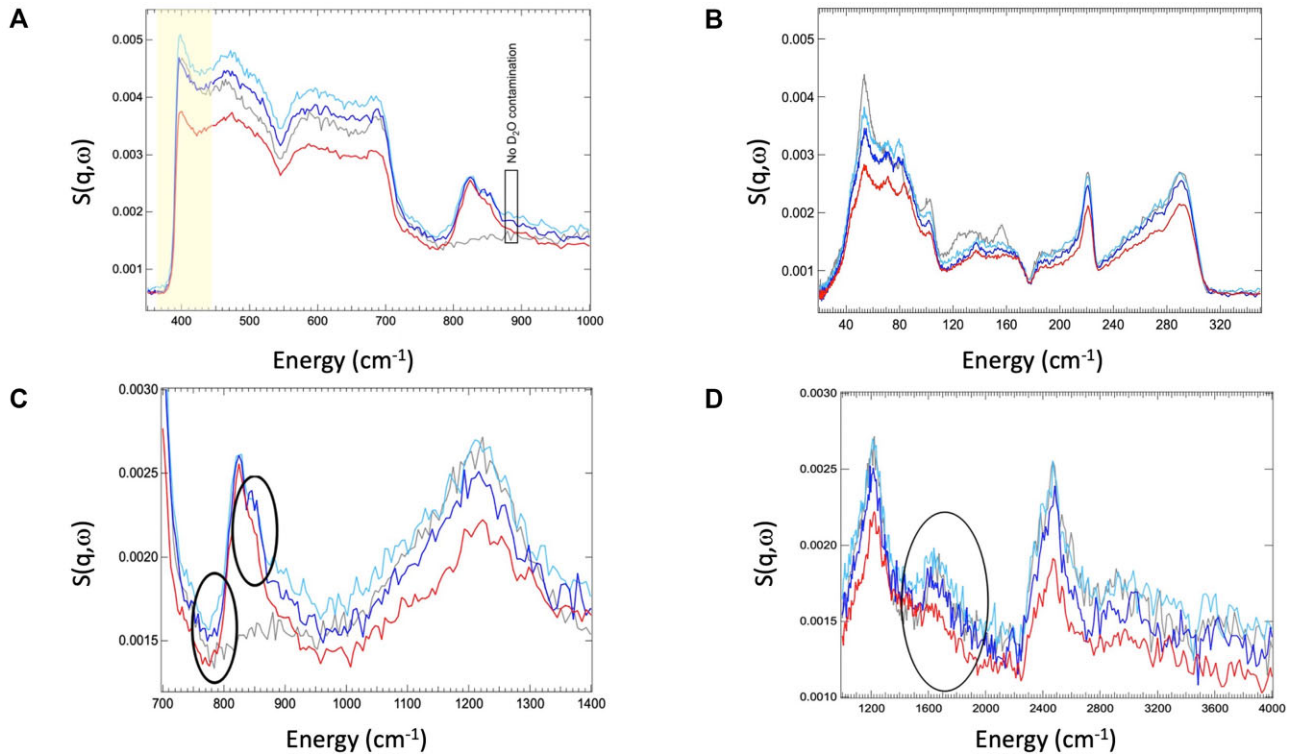


Figure 5. INS spectra. Spectra were collected at 10 K all in D_2O for deuterated crystalline ice Ih (gray), DNA (cyan), Hfq-CTR (blue), and Hfq-CTR:DNA complex (red), normalized to the elastic line to account for differences in density and instrument conditions. Here one should consider possible shifts due to harmonic, isotope-independent force constants, with a factor of $\sqrt{(20/18)} = 1.054$ for the translational modes. **(A)** No exchange with D_2O occurs, as indicated by the absence of a vibrational mode $\sim 900\text{ cm}^{-1}$ [50]. The softening of the 400 cm^{-1} vibration for the complexes, highlighted in yellow, indicates that hydration water remains undisturbed. **(B)** Lattice vibrations. The analysis of the overall spectral weight (or intensity) allows the conclusion that the fiber in D_2O is the stiffest. **(C)** Spectral changes suggest the partial opening of the dsDNA and an effect of the Hfq-CTR on the deoxyribose pucker, as described in the text. **(D)** The strong vibrational mode at 1625 cm^{-1} demonstrates interactions between Hfq-CTR and the N_6 amino group of adenines. An interaction at the N_6 position of adenine is typically indicative of major groove recognition [57]. This major groove interaction is further supported by the fact that A-tract DNA has a compressed, narrow minor groove, which is unlikely to accommodate an amyloid structure.

fore, any changes in the low-frequency spectral region reflect pure differences in DNA conformation [51]. From the analysis of the intensity of the lattice vibrational modes between 40 and 320 cm^{-1} (Fig. 5B), which also reflects the behavior of the Debye–Waller factor (U_{total}), we can conclude that the fiber in D_2O is stiffer than the isolated Hfq-CTR, which, in turn, is stiffer than the DNA (both in D_2O). This clearly confirms that fiber formation during the conformational transition of DNA bound to Hfq-CTR leads to greater structuring and rigidification of the complex compared to the peptide or DNA alone.

Additionally, the shoulder $\sim 800\text{ cm}^{-1}$ in the spectrum of the DNA complex (Fig. 5C) can be attributed to the simultaneous presence of free adenines and thymines (bands at 798 and 777 cm^{-1} , respectively), as well as adenines and thymines involved in H-bonding (absorptions at 793 and 770 cm^{-1} , respectively) [52]. This suggests that the bifurcation observed using cryo-EM is likely due to partial opening of the dsDNA. Our data also confirm the effect of the Hfq-CTR on the deoxyribose pucker. The spectral change in the $841\text{--}900\text{ cm}^{-1}$ range can be related to sugars that have undergone an S- to N-type puckering in the presence of the Hfq-CTR [52]. Additionally, the change in intensity between 1000 and 1300 cm^{-1} might indicate that the protein induces dehydration of the DNA, which could explain the sugar re-puckering observed. Finally, the strong vibrational mode observed in the Hfq-CTR

at approximately 1625 cm^{-1} (Fig. 5D) is assigned to an ND_2 bending coupled with a ring vibration of adenine. The softening and decreased intensity observed in the complex suggest an interaction between Hfq-CTR and the N_6 amino group of adenines [52].

The combined AFM, cryo-EM, SANS, and INS structural results have led us to propose a model for the fibrillar complex of Hfq-CTR and DNA (Fig. 6). In this model, the DNA helices in the complex are initially positioned provisionally (Fig. 6A). Constraints were then applied to refine the model shown in Fig. 6B, including (i) the hexagonal lattice; (ii) DNA helices with a diameter of 2 nm ; (iii) a helix spacing of $\sim 3.8\text{ nm}$; (iv) peptides surrounding the DNA (up to 3.3 nm), slightly deformed outwards; (v) the Hfq-CTR peptides were manually positioned between the DNA double helix monomers, taking into account the region necessary to form the amyloid structure, namely six ($S_{88}AQNTSAQQDS_{98}$) sequences that interact with each other [23]; (vi) residues previously identified to bind DNA (S_{65} , R_{66} , S_{69} , H_{70} , H_{71} , S_{72} , G_{76} , G_{77} , G_{78} , S_{80} , S_{81} , H_{84} , and H_{85}) [24]; (vii) the total diameter of the fiber of $\sim 16\text{ nm}$; and (viii) the N-terminal domains (NTR) of full-length Hfq, not present here but present in the full protein, extending outside the fiber. Both cryo-EM and INS experiments suggest that the dsDNA can locally separate into single strands. Figure 6A and C illustrates this specific region of the complex.

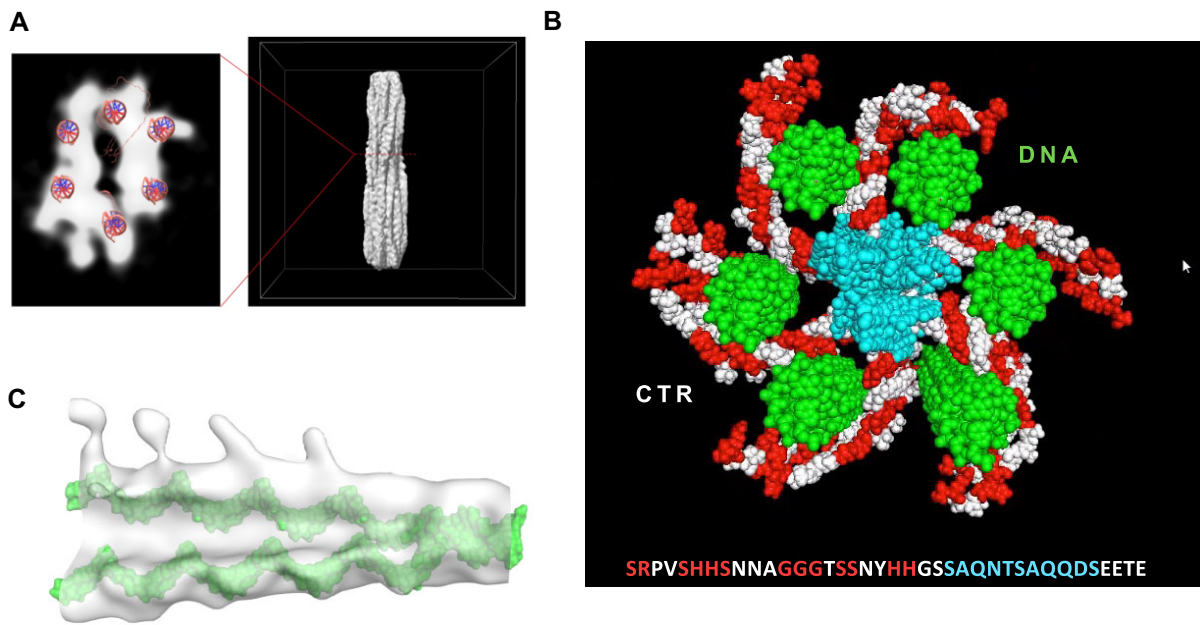


Figure 6. Fibrillar complexes of Hfq-CTR and DNA. **(A)** Approximate positions of the centers of mass of the DNA helices in the complex used in the modeling. This graph shows the cross-sectional view from the top of the complex along the fiber axis. Note that the hole at the center of panel (A) might indicate a depletion in density rather than complete absence of Hfq-CTR at this specific cross-section of the fiber (see the radial density profile of Hfq-CTR in Fig. 4F). **(B)** The six green DNA double-helices arranged hexagonally in this panel correspond to the positions of the six DNAs in panel (A) after refinement. The six N-terminal torus of Hfq, which are absent in this model, should decorate the fiber and extend outward from it. **(C)** As suggested by both Cryo-EM and INS experiments, the dsDNA can be locally separated into two single-stranded DNA regions. This specific region was also modeled in the Cryo-EM envelope.

Discussion

Both in eukaryotes and prokaryotes, maintaining DNA organization is crucial for genetic expression. While bacteria do not have histones, NAP proteins help to organize the bacterial chromatin. A common feature of several DNA architectural proteins is their ability to bridge DNA. Examples include the histone-like nucleoid structuring protein H-NS, which links distant DNA regions [53]. In this study, we focus on the structural characteristics of another DNA-bridging protein, the bacterial Hfq. Hfq, which is best known for its role in RNA-related processes, can also link two distant DNA regions, resulting in genome compaction [8,28]. Structurally, the organization of bridging proteins is typically conserved and consists of two modules: an oligomerization domain and a DNA-binding domain [54]. In the H-NS family, oligomerization usually relies on the formation of a “coiled-coil” dimerization motif, a feature common to H-NS as well as its homologs (MvaT, Rok...) [54]. H-NS can sequentially form two types of protein–DNA complexes, a nucleoprotein fiber and a bridged complex [54]. We showed that this model also applies to Hfq. First, Hfq scans the DNA to locate a specific site, typically an A-rich sequence [55, 56]. The amyloid domain of Hfq induces cooperative binding, increasing the protein’s affinity for DNA [15]. This cooperative binding enables the full protein to spread along the DNA, forming a nucleoprotein filament via its amyloid CTR, which likely interacts with recognition determinants in the DNA major groove [57]. This process, typically referred to as propagation, is likely to occur *in vivo*, as suggested by previous imaging studies [58]. Ultimately, these nucleoprotein filaments can interact with each other, facilitating the formation of bridges between distant DNA regions. While single-particle cryo-EM provides valuable insights into the

structure of individual fibers, a more comprehensive understanding of their arrangement and winding within the entire fiber structure requires tomography, which allows the study of fibers in their broader context. Notably, we observe that the fibers tend to adopt a specific arrangement into bundles (Supplementary Fig. S4).

However, an important question remains: does a post-translationally matured form of full-length Hfq exist, potentially leading to a free amyloid CTR that is resistant to proteases *in vivo*? Testing this hypothesis is challenging due to the lack of specific antibodies targeting the amyloid form of the CTR.

It is also important to note that DNA-bridging proteins can be classified into two categories: passive DNA bridgers, such as H-NS, which bind to distant DNA sequences and bring them together, and active DNA-bridging proteins, such as the SMC (structural maintenance of chromosomes) proteins, which use ATP hydrolysis to translocate along DNA. The presence of an ATP-binding site in Hfq and its ability to slide along DNA [59, 60] raises the question of whether Hfq could function as an active DNA-bridger. Moreover, Hfq is known to respond to various stresses encountered during bacterial life [61], making it intriguing to explore how environmental conditions might influence its DNA-bridging properties. Temperature, for instance, could significantly impact the self-assembly of the amyloid structure [62]. Finally, chemical modifications such as DNA methylation or post-translational modifications (PTMs) could play a role in the DNA compaction process. While PTMs have been identified in bacterial NAPs and Hfq [63, 64], their functional significance remains largely unknown, yet they could have a major impact on the structure and function of the

Hfq:DNA complex. These hypotheses will require further investigation.

In conclusion, the results herein seem to reveal a novel mechanism of DNA bridging that may be important for genome organization and the regulation of gene expression in prokaryotes, and likely important for eukaryotes. We identify a unique mechanism in which a NAP binds DNA edge-on and oligomerizes into amyloid filaments, rather than wrapping DNA around its surface like in eukaryotic nucleosomes.

Conclusion

While the exact mechanisms of chromosome compaction vary across organisms, the structural organization of DNA is conserved for maintaining genomic integrity. Both eukaryotic and prokaryotic cells rely on a combination of macromolecular assemblies to ensure optimal DNA compaction. This study highlights a unique mechanism in which a DNA-shaping protein binds DNA edge-on and oligomerizes into amyloid fibers, rather than wrapping DNA around its surface as seen in eukaryotic nucleosomes. Our results reveal a novel mechanism of DNA bridging and provide new perspectives on genome shaping and gene expression regulation in prokaryotes. This mechanism may also apply to eukaryotes, where amyloids have been discovered. These findings challenge the traditional understanding of how proteins, using amyloid domains, may organize and compact DNA.

Acknowledgements

The authors acknowledge the support of the European Union (EU) and Horizon 2020 through the iNEXT-Discovery Proposal (871037, Access Project PID: 19663), as well as the CRIOMECCORR project (ESFRI-2019-01-CSIC-16) for access to the CryoEM CNB-CSIC facility, and in particular, the assistance of Noelia Zamarreño. This work also benefited from access to the Instruct Image Processing Centre, an Instruct-ERIC centre, with financial support provided by Instruct-ERIC (PID 23014). We are thankful to ILL (Grenoble, France) for attribution of beamtime (proposal 85028). We gratefully acknowledge the Science and Technology Facilities Council (STFC) for access to TOSCA neutron beamtime at ISIS, as well as for the provision of sample preparation (proposal RB2000225). We are grateful to Sylvain Trepout (Monash University, Australia) for his help at an early stage of this work. We finally thank Sergio Marco (Sanofi, France), Jose-Maria Carazo and Carlos-Oscar Sorzano (CNB Madrid, Spain) for many fruitful discussions and Richard Sinden (SMDT, USA) for critical reading of the manuscript.

Author contributions: Conceptualization: V.A., J.P., F.W., and J.v.d.M.; Methodology: F.W., M.G., T.M., G.M., M.T.B., R.A., A.C., A.M., H.B., S.R., M.V., J.v.d.M., J.P., and V.A.; Software: M.G., T.M., G.M., A.M., and J.v.d.M.; Formal analysis: V.A. and J.v.d.M.; Investigation: F.W., M.G., T.M., G.M., M.T.B., R.A., A.C., A.M., H.B., S.R., M.V., J.v.d.M., J.P., and V.A.; Resources: V.A.; Data curation: M.G., A.M., and H.B.; Writing—original draft preparation: J.P., J.v.d.M., and V.A.; Writing—review and editing: F.W., M.G., T.M., G.M., M.T.B., R.A., A.C., A.M., H.B., S.R., M.V., J.v.d.M., J.P., and V.A.; Visualization: G.M. and M.G.; Project administration: V.A.; Funding acquisition: V.A. All authors have read and agreed to the published version of the manuscript.

Supplementary data

Supplementary Data is available at NAR online.

Conflict of interest

The authors declare no conflict of interest.

Funding

J.v.d.M. acknowledges support from the Singapore Ministry of Education Academic Research Fund, Tier 2 (MOE-T2EP50121-0003). This study contributes to the IdEx Université Paris Cité ANR-18-IDEX-0001 (to V.A.). This work was also supported by a public grant overseen by the French National Research Agency (ANR) as part of the Investissements d’Avenir program, through the “ADI 2019” project funded by the IDEX Paris-Saclay, ANR-11-IDEX-0003-02 (to A.C.) and by the Fédération Française de Diffusion Neutronique (to J.P., T.M. and V.A.).

Data availability

Cryo-EM data (full and half maps) have been deposited on Electron Microscopy Data Bank (EMDB) under the access code EMD-52187 through the wwPDB OneDep System. SANS data are available from: <http://doi.ill.fr/10.5291/ILL-DATA.8-03-1038>. TOSCA data collected under proposal number RB2000225 are available upon request.

References

1. Kuzminov A. Bacterial nucleoid is a riddle wrapped in a mystery inside an enigma. *J Bacteriol* 2024;206:e0021123. <https://doi.org/10.1128/jb.00211-23>
2. Monk JM, Koza A, Campodonico MA *et al.* Multi-omics quantification of species variation of *Escherichia coli* links molecular features with strain phenotypes. *Cell Syst* 2016;3:238–51. <https://doi.org/10.1016/j.cels.2016.08.013>
3. Dorman CJ. Function of nucleoid-associated proteins in chromosome structuring and transcriptional regulation. *J Mol Microbiol Biotechnol* 2014;24:316–31.
4. Dame RT, Goosen N. HU: promoting or counteracting DNA compaction? *FEBS Lett* 2002;529:151–6. [https://doi.org/10.1016/S0014-5793\(02\)03363-X](https://doi.org/10.1016/S0014-5793(02)03363-X)
5. Owen-Hughes TA, Pavitt GD, Santos DS *et al.* The chromatin-associated protein H-NS interacts with curved DNA to influence DNA topology and gene expression. *Cell* 1992;71:255–65. [https://doi.org/10.1016/0092-8674\(92\)90354-F](https://doi.org/10.1016/0092-8674(92)90354-F)
6. Dorman CJ. H-NS: a universal regulator for a dynamic genome. *Nat Rev Micro* 2004;2:391–400. <https://doi.org/10.1038/nrmicro883>
7. Dame RT, Wyman C, Goosen N. H-NS mediated compaction of DNA visualised by atomic force microscopy. *Nucleic Acids Res* 2000;28:3504–10. <https://doi.org/10.1093/nar/28.18.3504>
8. Geinguenaud F, Calandrini V, Teixeira J *et al.* Conformational transition of DNA bound to Hfq probed by infrared spectroscopy. *Phys Chem Chem Phys* 2011;13:1222–9. <https://doi.org/10.1039/C0CP01084G>
9. Azam TA, Ishihama A. Twelve species of the nucleoid-associated protein from *Escherichia coli*. Sequence recognition specificity and DNA binding affinity. *J Biol Chem* 1999;274:33105–13. <https://doi.org/10.1074/jbc.274.46.33105>
10. Ishihama A. Modulation of the nucleoid, the transcription apparatus, and the translation machinery in bacteria for stationary phase survival. *Genes Cells* 1999;4:135–43. <https://doi.org/10.1046/j.1365-2443.1999.00247.x>

11. Brennan RG, Link TM. Hfq structure, function and ligand binding. *Curr Opin Microbiol* 2007;10:125–33. <https://doi.org/10.1016/j.mib.2007.03.015>
12. Vogel J, Luisi BF. Hfq and its constellation of RNA. *Nat Rev Micro* 2011;9:578–89. <https://doi.org/10.1038/nrmicro2615>
13. Folichon M, Arluison V, Pellegrini O *et al.* The poly (A) binding protein Hfq protects RNA from RNase E and exoribonucleolytic degradation. *Nucleic Acids Res* 2003;31:7302–10. <https://doi.org/10.1093/nar/gkg915>
14. Updegrove TB, Correia JJ, Galletto R *et al.* E. coli DNA associated with isolated Hfq interacts with Hfq's distal surface and C-terminal domain. *Biochim Biophys Acta* 2010;1799:588–96. <https://doi.org/10.1016/j.bbagg.2010.06.007>
15. Malabirade A, Jiang K, Kubiak K *et al.* Compaction and condensation of DNA mediated by the C-terminal domain of Hfq. *Nucleic Acids Res* 2017;45:7299–308. <https://doi.org/10.1093/nar/gkx431>
16. Diestra E, Cayrol B, Arluison V *et al.* Cellular electron microscopy imaging reveals the localization of the Hfq protein close to the bacterial membrane. *PLoS One* 2009;4:e8301. <https://doi.org/10.1371/journal.pone.0008301>
17. Arluison V, Folichon M, Marco S *et al.* The C-terminal domain of *Escherichia coli* Hfq increases the stability of the hexamer. *Eur J Biochem* 2004;271:1258–65. <https://doi.org/10.1111/j.1432-1033.2004.04026.x>
18. Sun X, Zhulin I, Wartell RM. Predicted structure and phyletic distribution of the RNA-binding protein Hfq. *Nucleic Acids Res* 2002;30:3662–71. <https://doi.org/10.1093/nar/gkf508>
19. Schumacher MA, Pearson RF, Moller T *et al.* Structures of the pleiotropic translational regulator Hfq and an Hfq- RNA complex: a bacterial Sm-like protein. *Embo J* 2002;21:3546–56. <https://doi.org/10.1093/emboj/cdf322>
20. Sharma A, Dubey V, Sharma R *et al.* The unusual glycine-rich C terminus of the *Acinetobacter baumannii* RNA chaperone Hfq plays an important role in bacterial physiology. *J Biol Chem* 2018;293:13377–88. <https://doi.org/10.1074/jbc.RA118.002921>
21. Fortas E, Piccirilli F, Malabirade A *et al.* New insight into the structure and function of Hfq C-terminus. *Biosci Rep* 2015;35:e00190. <https://doi.org/10.1042/BSR20140128>
22. Berbon M, Martinez D, Morvan E *et al.* Hfq C-terminal region forms a beta-rich amyloid-like motif without perturbing the N-terminal Sm-like structure. *Commun Biol* 2023;6:1075. <https://doi.org/10.1038/s42003-023-05462-1>
23. Malabirade A, Morgado-Brajones J, Trepout S *et al.* Membrane association of the bacterial riboregulator Hfq and functional perspectives. *Sci Rep* 2017;7:10724. <https://doi.org/10.1038/s41598-017-11157-5>
24. Turbant F, EH O, Partouche D *et al.* Identification and characterization of the Hfq bacterial amyloid region DNA interactions. *BBA Adv* 2021;1:100029. <https://doi.org/10.1016/j.bbadv.2021.100029>
25. Malabirade A, Partouche D, El Hamoui O *et al.* Revised role for Hfq bacterial regulator on DNA topology. *Sci Rep* 2018;8:16792. <https://doi.org/10.1038/s41598-018-35060-9>
26. Arluison V, Mura C, Guzman MR *et al.* Three-dimensional structures of fibrillar Sm proteins: hfq and other Sm-like proteins. *J Mol Biol* 2006;356:86–96. <https://doi.org/10.1016/j.jmb.2005.11.010>
27. Jiang K, Zhang C, Guttula D *et al.* Effects of Hfq on the conformation and compaction of DNA. *Nucleic Acids Res* 2015;43:4332–41. <https://doi.org/10.1093/nar/gkv268>
28. Cossa A, Trepout S, Wien F *et al.* Cryo soft X-ray tomography to explore *Escherichia coli* nucleoid remodeling by Hfq master regulator. *J Struct Biol* 2022;214:107912. <https://doi.org/10.1016/j.jsb.2022.107912>
29. Orans J, Kovach AR, Hoff KE *et al.* Crystal structure of an *Escherichia coli* Hfq Core (residues 2-69)-DNA complex reveals multifunctional nucleic acid binding sites. *Nucleic Acids Res* 2020;48:3987–97. <https://doi.org/10.1093/nar/gkaa149>
30. Eisenberg DS, Sawaya MR. Structural studies of amyloid proteins at the molecular level. *Annu Rev Biochem* 2017;86:69–95. <https://doi.org/10.1146/annurev-biochem-061516-045104>
31. Li Q, Babinchak WM, Surewicz WK. Cryo-EM structure of amyloid fibrils formed by the entire low complexity domain of TDP-43. *Nat Commun* 2021;12:1620. <https://doi.org/10.1038/s41467-021-21912-y>
32. Krueger S. Small-angle neutron scattering contrast variation studies of biological complexes: challenges and triumphs. *Curr Opin Struct Biol* 2022;74:102375. <https://doi.org/10.1016/j.sbi.2022.102375>
33. Ohyagi Y, Asahara H, Chui DH *et al.* Intracellular Abeta42 activates p53 promoter: a pathway to neurodegeneration in Alzheimer's disease. *FASEB j* 2005;19:255–7. <https://doi.org/10.1096/fj.04-2637je>
34. Khmeleva SA, Radko SP, Kozin SA *et al.* Zinc-mediated binding of nucleic acids to amyloid-beta aggregates: role of histidine residues. *JAD* 2016;54:809–19. <https://doi.org/10.3233/JAD-160415>
35. Zheng SQ, Palovcak E, Armache JP *et al.* MotionCor2: anisotropic correction of beam-induced motion for improved cryo-electron microscopy. *Nat Methods* 2017;14:331–2. <https://doi.org/10.1038/nmeth.4193>
36. Punjani A, Rubinstein JL, Fleet DJ *et al.* cryoSPARC: algorithms for rapid unsupervised cryo-EM structure determination. *Nat Methods* 2017;14:290–6. <https://doi.org/10.1038/nmeth.4169>
37. Rohou A, Grigorieff N. CTFFIND4: fast and accurate defocus estimation from electron micrographs. *J Struct Biol* 2015;192:216–21. <https://doi.org/10.1016/j.jsb.2015.08.008>
38. Horcas I, Fernandez R, Gómez-Rodríguez M *et al.* WSXM: a software for scanning probe microscopy and a tool for nanotechnology. *Rev Sci Instrum* 2007;78:013705. <https://doi.org/10.1063/1.2432410>
39. Matsuo T, Arluison V, Wien F *et al.* Structural information on bacterial amyloid and amyloid-DNA complex obtained by small-angle neutron or X-ray scattering. *Methods Mol Biol* 2022;2538:75–93. https://doi.org/10.1007/978-1-0716-2529-3_6
40. Zakharova SS, Egelhaaf SU, Bhuiyan LB *et al.* Multivalent ion-DNA interaction: neutron scattering estimates of polyamine distribution. *J Chem Phys* 1999;111:10706–16. <https://doi.org/10.1063/1.480425>
41. Dai L, Mu Y, Nordenskiöld L *et al.* Molecular dynamics simulation of multivalent-ion mediated attraction between DNA molecules. *Phys Rev Lett* 2008;100:118301. <https://doi.org/10.1103/PhysRevLett.100.118301>
42. Pinna RS, Rudić S, Parker SF *et al.* The neutron guide upgrade of the TOSCA spectrometer. *Nucl Instrum Methods Phys Res A* 2018;896:68–74. <https://doi.org/10.1016/j.nima.2018.04.009>
43. Arnold O, Bilheux JC, Borreguero JM *et al.* Mantid—data analysis and visualization package for neutron scattering and μ SR experiments. *Nucl Instrum Methods Phys Res A* 2014;764:156–66. <https://doi.org/10.1016/j.nima.2014.07.029>
44. Sears V. Neutron scattering lengths and cross sections. *Neutron News* 1992;3.3:26–37. <https://doi.org/10.1080/10448639208218770>
45. Smith J, Cusack S, Tidor B *et al.* Inelastic neutron scattering analysis of low-frequency motions in proteins: harmonic and damped harmonic models of bovine pancreatic trypsin inhibitor. *J Chem Phys* 1990;93:2974–91. <https://doi.org/10.1063/1.458885>
46. Mitchell CH, Parker SF, Ramirez-Cuesta A *et al.* Vibrational Spectroscopy with Neutrons with Applications in Chemistry, Biology, Materials Science and Catalysis. In: *Series on Neutron Techniques and Applications*. Vol. 3, World Scientific, 2005.
47. Pettersen EF, Goddard TD, Huang CC *et al.* UCSF Chimera—a visualization system for exploratory research and analysis. *J Comput Chem* 2004;25:1605–12. <https://doi.org/10.1002/jcc.20084>

48. van der Maarel JRC. Form factor of helical structures and twisted fibres. *J Appl Crystallogr* 2023;56:1714–20. <https://doi.org/10.1107/S1600576723008671>
49. Pezzotti S, Sebastiani F, van Dam EP *et al.* Spectroscopic fingerprints of cavity formation and solute insertion as a measure of hydration entropic loss and enthalpic gain. *Angew Chem Int Ed* 2022;61:e202203893. <https://doi.org/10.1002/anie.202203893>
50. Li J. Inelastic neutron scattering studies of hydrogen bonding in ices *J Chem Phys* 1996;105:6733–55. <https://doi.org/10.1063/1.472525>
51. Lamba OP, Wang AH, Thomas GJ Jr. Low-frequency dynamics and Raman scattering of crystals, of B-, A-, and Z-DNA, and fibres of C-DNA. *Biopolymers* 1989;28:667–78. <https://doi.org/10.1002/bip.360280210>
52. Balduzzi E, Geinguenaud F, Sordyl D *et al.* NAIRDB: a database of Fourier transform infrared (FTIR) data for nucleic acids. *Nucleic Acids Res* 2024;53:D157–D162. <https://doi.org/10.1093/nar/gkae885>
53. Wiggins PA, Dame RT, Noom MC *et al.* Protein-mediated molecular bridging: a key mechanism in biopolymer organization. *Biophys J* 2009;97:1997–2003. <https://doi.org/10.1016/j.bpj.2009.06.051>
54. Qin L, Erkelens AM, Ben Bdira F *et al.* The architects of bacterial DNA bridges: a structurally and functionally conserved family of proteins. *Open Biol* 2019;9:190223. <https://doi.org/10.1098/rsob.190223>
55. Easo George J, Basak R, Yadav I *et al.* Effect of base methylation on binding and mobility of bacterial protein Hfq on double-stranded DNA. *Lab Chip* 2024;24:5137–44. <https://doi.org/10.1039/D4LC00628C>
56. Tan CJ, Basak R, Yadav I *et al.* Mobility of bacterial protein Hfq on dsDNA: role of C-terminus-mediated transient binding. *J Phys Chem B* 2022;126:1477–82. <https://doi.org/10.1021/acs.jpccb.1c10234>
57. Xiong Y, Sundaralingam M. *eLS*. Hoboken, New Jersey, USA: Macmillan Publishers Ltd, Nature Publishing Group, 2001.
58. Cech GM, Szalewska-Palasz A, Kubiak K *et al.* The *Escherichia coli* Hfq Protein: an unattended DNA-transactions regulator. *Front Mol Biosci* 2016;3:36. <https://doi.org/10.3389/fmolb.2016.00036>
59. Arluison V, Mutyam SK, Mura C *et al.* Sm-like protein Hfq: location of the ATP-binding site and the effect of ATP on Hfq–RNA complexes. *Protein Sci* 2007;16:1830–41. <https://doi.org/10.1110/ps.072883707>
60. Yadav I, Basak R, Yan P *et al.* Role of internal DNA motion on the mobility of a nucleoid associated protein. *J Phys Chem Lett* 2020;11:8424–8429. <https://doi.org/10.1021/acs.jpcclett.0c02251>
61. Gottesman S. Trouble is coming: signaling pathways that regulate general stress responses in bacteria. *J Biol Chem* 2019;294:11685–700. <https://doi.org/10.1074/jbc.REV119.005593>
62. Ow SY, Dunstan DE. The effect of concentration, temperature and stirring on hen egg white lysozyme amyloid formation. *Soft Matter* 2013;9:9692–701. <https://doi.org/10.1039/c3sm51671g>
63. Dilweg IW, Dame RT. Post-translational modification of nucleoid-associated proteins: an extra layer of functional modulation in bacteria? *Biochem Soc Trans* 2018;46:1381–92. <https://doi.org/10.1042/BST20180488>
64. Obregon KA, Hoch CT, Sukhodolets MV. Sm-like protein Hfq: composition of the native complex, modifications, and interactions. *Biochim Biophys Acta* 2015;1854:950–66. <https://doi.org/10.1016/j.bbapap.2015.03.016>